

Efficient Excitation of High-Purity Modes in Arbitrary Waveguide Geometries

Ralf Mouthaan^{*†}, Peter Christopher[†], Jonathan Pinnell^{*}, Michael Frosz[‡], George Gordon[§], Timothy Wilkinson[†], Tijmen G. Euser^{*}

^{*}Nanophotonics Centre, Cavendish Laboratory (University of Cambridge, UK), [†]CAPE (University of Cambridge, UK)

[‡]Max Planck Institute for the Science of Light (Erlangen, Germany)

[§]Electrical Engineering Department (University of Nottingham, UK)

Abstract—A general method is presented for exciting discrete modes in waveguides of arbitrary geometry. Guided modes supported by the waveguide are first calculated using a finite difference frequency domain model. High efficiency holograms to excite these discrete modes are then generated using the Direct Search hologram generation algorithm. The Direct Search algorithm is optimised such that the inherent properties of waveguide modes are exploited to give faster execution times. A nodeless antiresonant photonic crystal fibre is considered as a test geometry, in which high-purity modes are experimentally excited and in-coupling efficiencies of up to 32.8% are obtained.

I. INTRODUCTION

The excitation of discrete modes in optical waveguides has long been of interest for modal multiplexing for telecommunications [1]–[3]. More recently, discrete mode excitation has been used to create conveyor belts of optically trapped microparticles [4], for stimulated Raman amplification of selectively-excited higher-order modes [5], and for atomic spectroscopy [6].

Waveguide modes can be excited by coupling light into the waveguide via a side-mounted prism [7]–[9] or grating [10]–[12]. Matching the wavevector of the incident light with the wavevector of a guided mode allows an individual mode to be excited. Alternatively, a single mode fibre (SMF) can be spliced to a multimode fibre (MMF), positioned such that a group of modes are selectively excited [13]–[15]. Photonic lanterns build on this, and consist of a number of SMFs spliced to a MMF via a gradual taper [16]–[18]. Light propagating into a given SMF couples to other SMFs over the length of the transition, forming a spatial profile that couples into a target MMF mode.

The use of phase masks for mode excitation was introduced by Berdagué & Facq [19]. These allow the magnitude and phase of the incident light field to be tailored such that coupling into a target mode is optimised. The introduction of the spatial light modulator has popularised these wavefront shaping techniques [2], [3], [20]–[23], permitting modes to be excited with high purity, facilitating fine alignment and aberration correction, and allowing the excited mode to be dynamically changed on the fly. Wavefront shaping techniques have been used to excite discrete modes in step index fibre [21], [22], graded index fibre [2], [3], [23], and photonic crystal fibre (PCF) [24], [25]. Similarly, wavefront shaping

techniques could soon be used to excite discrete modes in other geometries such as double-clad fibres, ring-core fibres, multi-core fibres and elliptical fibres.

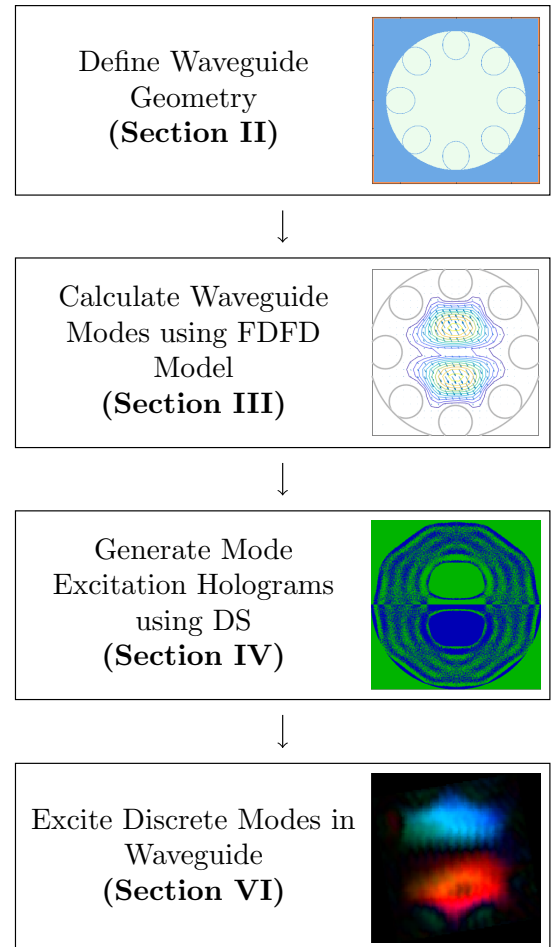


Fig. 1: Flow chart describing the procedure for exciting discrete modes in arbitrary waveguide geometries.

Previous work exciting discrete modes in PCFs has estimated the spatial profiles of the guided modes by approximating their structure to that of a hollow cylinder [24], [25]. This paper takes a more rigorous approach, using a full-wave finite difference model to more accurately estimate the modes guided by the waveguide in question (Section III). While

the techniques presented can be applied to any waveguide geometry, an antiresonant nodeless HC-PCF (introduced in Section II) is used as an example geometry. It is emphasised that any other geometry could equally be considered.

Holographic wavefront shaping techniques are then used to excite the HC-PCF modes. Fourier holograms are generated to excite these modes using a Direct Search (DS) algorithm introduced in Section IV. This algorithm allows all modes in the waveguide to be excited with exceptionally high efficiencies. Intrinsic properties of the waveguide modes are exploited to speed up the execution of the algorithm. Finally, experimental excitation of modes in the test geometry is demonstrated in Section VI. The work flow introduced by this paper is illustrated in Fig. 1.

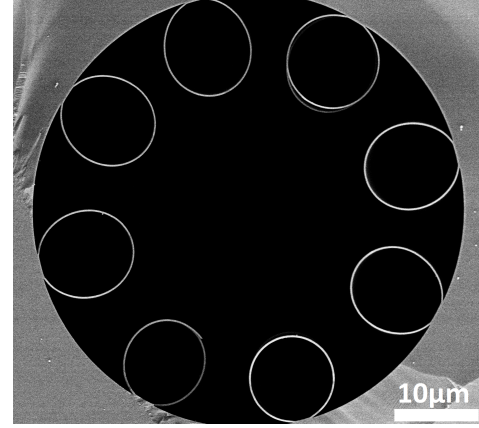
II. WAVEGUIDE UNDER TEST

Photonic crystal fibres (PCFs) break the optical waveguide mould by using mechanisms other than total internal reflection to guide light. Instead, their guidance properties are derived from their complex transverse structure. PCFs can be tailored to offer unique properties such as broadband light guidance [26], high power light guidance [27], extremely low-loss light guidance [28]. These waveguides allow light to be guided within a hollow, gas-filled or liquid-filled core with a low refractive index. This has enabled their use as chemical microreactors [29] and for gas-based nonlinear optics [30].

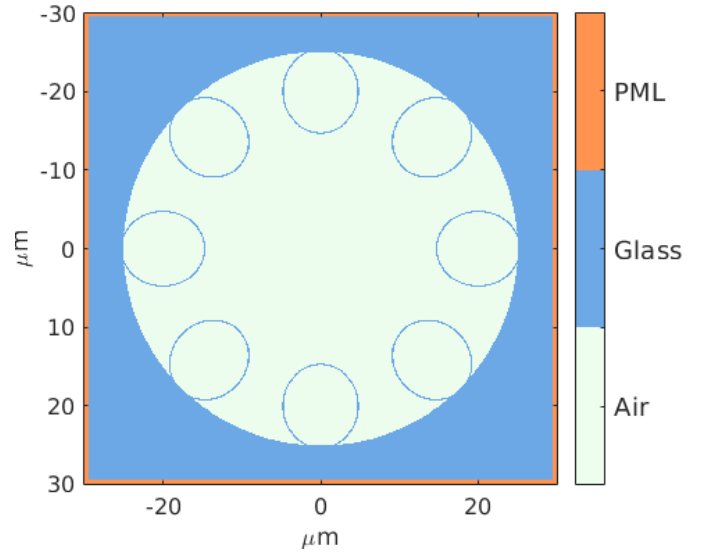
An antiresonant nodeless PCF [31] has been selected for use here, the guidance mechanism of which is based on antiresonant reflection [32]. The structure of these waveguides is significantly simplified compared to that of conventional HC-PCFs. Antiresonant HC-PCFs have seen significant interest recently, showing promising low-loss guidance results [28], [33]–[35] and exhibiting interesting polarisation maintaining properties [36]. The specific fibre used was drawn at the Max Planck Institute for the Science of Light in Erlangen, Germany. While the waveguide is not optimised for use at the 633nm wavelength considered, it does serve to illustrate the techniques presented can be used to excite discrete modes in any arbitrary waveguide geometry.

To prevent artefacts related to the binarisation of the SEM image, the computational model was generated using an idealized structure based on the measured fibre dimensions, as shown in Fig. 2b. The ‘glass’ regions were assigned a refractive index of 1.45, and the ‘air’ regions were assigned a refractive index of 1.00. Here, propagation invariant modes are calculated and excited at 633nm, corresponding to the operating wavelength of the helium-neon laser used. The ARROW model [32], [37] predicts that this wavelength lies between a guiding antiresonance at 840nm and a lossy resonance at 420nm, where a wall thickness of 200nm and a glass refractive index of 1.45 have been assumed.

The PCF used as the waveguide under test is cleaved to a length of approximately 8cm. Care is taken to achieve as flat a cleave as feasible, as it is not possible to subsequently polish the fibre facet. Any unwanted distortions of the fibre facet will lead to local perturbation of the guided modes, as well as distortion of the incident wavefront. Cross-mode coupling,



(a) Scanning electron micrograph of the fibre facet



(b) Computational model of the PCF geometry

Fig. 2: Geometry of the antiresonant nodeless PCF used as test geometry. A 50µm diameter hollow core is lined with eight smaller capillaries. The smaller capillaries are slightly elliptical, with a major axis of 10.5µm and a minor axis of approximately 9.7µm. The capillaries have a wall thickness of approximately 200nm.

bend losses and modal losses are minimised by using a short length of fibre, by mounting the waveguide in V-groove such that it is held perfectly straight, and by securing it in place using a small section of tape so that there are no stresses or strains exerted on the waveguide.

III. MODE CALCULATION

Firstly, the modes guided by the waveguide need to be determined. The complex structure of a PCF can be approximated to a hollow capillary, which allows the real part of the modal propagation constant to be estimated [38] and the modes guided by the PCF to be approximated to linearly polarised (LP) modes [24]. These approximate modes can then be excited using incident Laguerre-Gauss modes. This approach may omit modes that do not have an LP counterpart [25], or modes may be predicted to guide that do not do so in practice. Additionally, it is likely that imperfect estimates of the mode profile will not allow the mode to be subsequently excited with

high purity. Although this approximation is widely used, it is not robustly generalisable to the increasingly wide range of fibre geometries in use.

A full-wave finite difference frequency domain (FDFD) electromagnetic model has been developed. The FDFD model will more accurately study the behaviour of the waveguide in question by eliminating the hollow capillary approximation previously used [24], [25]. It is also possible to use commercial electromagnetic solvers, such as Lumerical's MODE solver [39] or COMSOL's multi-physics solver for this calculation [40], or open source electromagnetic solvers such as MEEP [41].

Assuming sinusoidal time dependence $e^{i\omega t}$ where t is time and ω denotes the angular frequency, the electromagnetic fields can be described by Eqs. 1 and 2, which relate the vector electric field \mathbf{E} to the vector magnetic field \mathbf{H}

$$\nabla \times \mathbf{E} = -i\omega\mu\mathbf{H} \quad (1)$$

$$\nabla \times \mathbf{H} = i\omega\epsilon\mathbf{E} \quad (2)$$

Recognising that a waveguide is translationally invariant, the fields are seen to vary along the axis z as $e^{i\beta z}$ where β is the mode propagation constant. This allows any derivatives with respect to z to be eliminated and Maxwell's curl equations to be expressed as a two-dimensional problem. The fields can be expressed on a Yee cell that has been modified for the two-dimensional case, as shown in Fig. 3, and any spatial derivatives can then be expressed using a central differencing scheme. Permittivities are defined at the centre of each Yee cell, and so central differencing can also be used to obtain permittivity estimates at the other Yee cell nodes. To avoid reflections from the boundary, perfectly matched layer (PML) absorbing boundary conditions have been implemented at the edges of the problem space (shown in Fig. 2b). These have been implemented using a coordinate transformation [42].

Following the example of Zhu & Brown [43] and Yu & Chang [44], the problem can then be manipulated to yield an eigenvalue equation. The refractive indices of the materials used here are isotropic, and are described by a diagonal permittivity matrix. A simple eigenvalue equation can hence be defined in terms of only the magnetic fields, as shown in Eq. 3 where M_H describes the relationship between fields at different points on the mesh.

$$M_H \begin{bmatrix} H_x \\ H_y \end{bmatrix} = \beta^2 \begin{bmatrix} H_x \\ H_y \end{bmatrix} \quad (3)$$

This equation has been implemented using sparse matrices, and the eigenvalues and eigenvectors found using the Arnoldi iteration algorithm. Each obtained eigenvalue-eigenvector pair corresponds to a single guided mode. The modal propagation constant can be determined from an eigenvalue, and H_x and H_y field profile of the modes can be determined from the corresponding eigenvector. The E_x , E_y , E_z and H_z field profiles can subsequently be calculated from the H_x and H_y fields using Maxwell's equations. The Arnoldi algorithm is capable of finding tens to hundreds of eigenvalue-eigenvector pairs with eigenvalues close to an estimated value β_0^2 . An

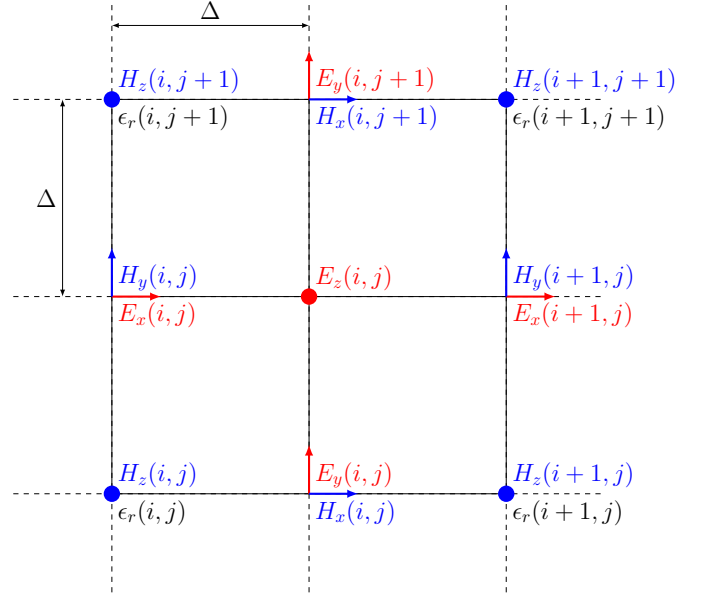


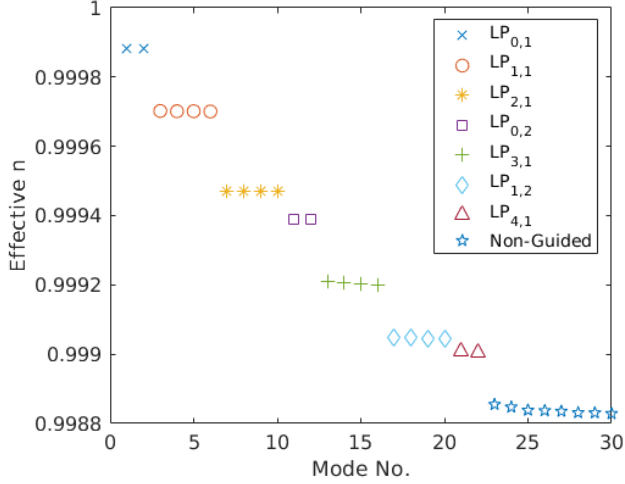
Fig. 3: The Yee cell gives a spatially staggered representation of the electric and magnetic field components. By assuming the waveguide to be translationally invariant, a modified two-dimensional Yee cell can be formulated, as shown here.

estimated value of $\beta_0 = 2\pi/\lambda$ is used as this approximates the propagation constant of the fundamental mode.

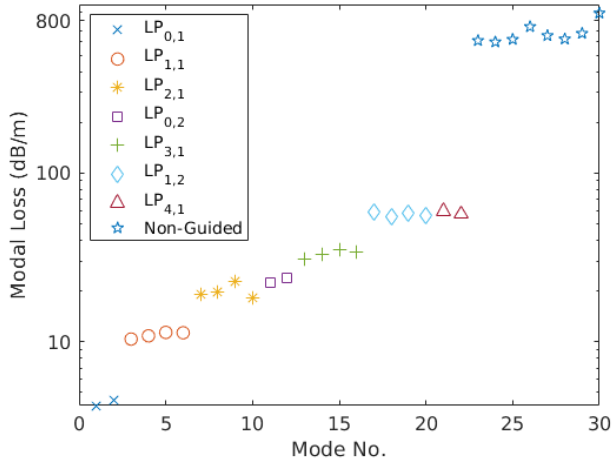
The presented FDFD model has been implemented in MATLAB and made available at [45]. It has been validated against theoretical values obtained for the analytically tractable step index waveguide geometry, as well as published propagation constant and loss values [43], [46]–[48]. The FDFD model has been used to model the waveguide under test presented in Section II. A $60\mu\text{m} \times 60\mu\text{m}$ problem space is modelled using a 1000×1000 cells, giving a sufficiently fine mesh with $\lambda/dx \approx 10.5$. A 10-pixel PML with a cubic loss function has been implemented at the edges, giving an attenuation factor of approximately 10^{-5} . The eigensolver was used to find the first 30 modes supported by this geometry. This number was selected through trial and error, and it shall be shown that this allows all guided modes along with a handful of non-guided modes to be captured. The waveguide under test has also been modelled using Lumerical's MODE solver [39] and effective mode refractive indices were found to agree with the presented model to within 3×10^{-6} .

The imaginary components of the obtained propagation constants are shown in Fig. 4b, showing that only 22 modes are guided in this waveguide at this wavelength. The fundamental mode exhibits a loss of approximately 4.2 dB/m, whereas the highest-order $\text{LP}_{4,1}$ guided modes exhibit high losses of 59 dB/m. It is noted that the operating wavelength falls in the first guidance window of the waveguide (i.e. between the first two lossy resonances), which typically exhibits the highest confinement loss.

Inspection of the real components of the propagation constants, shown in Fig. 4a, reveals that the guided modes can be divided into 7 groups of degenerate modes. Most of the mode profiles indicate the calculated modes are linearly polarised.



(a) Mode effective refractive index.



(b) Mode Loss.

Fig. 4: Effective refractive index and loss of the modes guided in the antiresonant nodeless PCF geometry considered. These have been calculated from the real and imaginary components of the modal propagation constants.

This is occasionally not the case though, for example for the second degenerate mode group, marked by circles in Fig. 4 and illustrated in Figs. 5a to 5d. When this is not the case, separate modes can be superimposed to yield equivalent linearly polarised modes, as shown in Figs. 5e to 5h. The superpositions have been made in such a way that the orthogonality of the modes has been conserved. In this manner, it has been possible to obtain a complete set of linearly polarised modes as shown in Fig. 9, which will act as the target fields to be projected by the holograms displayed on the SLM. In the interest of brevity only one mode from each mode group will be considered from this point on, but each of the corresponding degenerate modes, consisting of spatially rotated or polarisation rotated counterparts, are also guided and can also be excited.

IV. HOLOGRAM GENERATION

A hologram displayed on a commercially available nematic liquid crystal on silicon spatial light modulator (SLM) can

modulate the phase of incident light, but is not able to modulate its amplitude. Taking this into consideration, a hologram $H(x, y)$ needs to be computed such that the light diffracted by the hologram creates a replay field $R(u, v)$ in the fibre facet plane that excites the target mode. A number of approaches have been proposed, including double-phase holograms [49] and techniques that exploit the use of spatial filters in the Fourier plane [21], [24], [25]. Here, a Fourier hologram will be considered that is optimised using a Direct Search (DS) algorithm [2], [50], [51].

The SLM is positioned at one focal plane of a lens and the proximal fibre facet is positioned at the opposite focal plane of the lens. A Fourier transform relationship then exists between the fields in the SLM plane and the replay field in the fibre facet plane, in addition to a linear coordinate scaling [52]:

$$R(u, v) = \frac{1}{i\lambda f} \int_{-\infty}^{\infty} \int_{-\infty}^{\infty} H(x, y) e^{-\frac{i2\pi}{\lambda f}(xu+yv)} dx dy. \quad (4)$$

The SLM plane is naturally discretised into pixels, and so also discretising the replay field plane allows this relationship to be expressed as a discrete Fourier transform, as shown in Eq. 5, where the hologram and the replay field are both of dimensions $N_x \times N_y$. Coordinates have been normalised in this case to eliminate any scaling factors. The replay field is then given by

$$R(u, v) = \frac{1}{\sqrt{N_x N_y}} \sum_{x=0}^{N_x-1} \sum_{y=0}^{N_y-1} H(x, y) e^{2\pi i \left(\frac{ux}{N_x} + \frac{vy}{N_y} \right)} \quad (5)$$

Considering a target scalar mode profile $T(u, v)$ calculated using the FDFD model described previously, the target mode will be excited by a replay field that maximises the overlap integral error metric Err_{Overlap} of Eq. 6, where summations are performed over all pixels within a region of interest ROI. The ROI is chosen to be 50% larger than the region containing the PCF core and surrounding capillaries, so in this case consists of a circle with a diameter of $75\mu\text{m}$. Light incident on the fibre facet outside of this ROI will not couple into any guided mode. Including a ROI provides the DS algorithm with further degrees of freedom, allowing a more optimal solution to be found. The modes guided by a waveguide are orthogonal, and so maximising the overlap integral for the target mode corresponds to minimising the overlap integral for all other modes:

$$Err_{\text{Overlap}} = \frac{\left| \sum_{\text{ROI}} RT^* \right|^2}{\sum_{\text{ROI}} |T|^2 \sum_{\text{ROI}} |R|^2} \quad (6)$$

As much power as possible is to be coupled into the target mode. The amount of power coupled into the target mode Err_{Power} is calculated using the following expression, where \sum_{∞} is the sum performed over all pixels, i.e. not just those within the ROI.

$$Err_{\text{Power}} = \frac{\sum_{\text{ROI}} |R|^2}{\sum_{\infty} |R|^2} \quad (7)$$

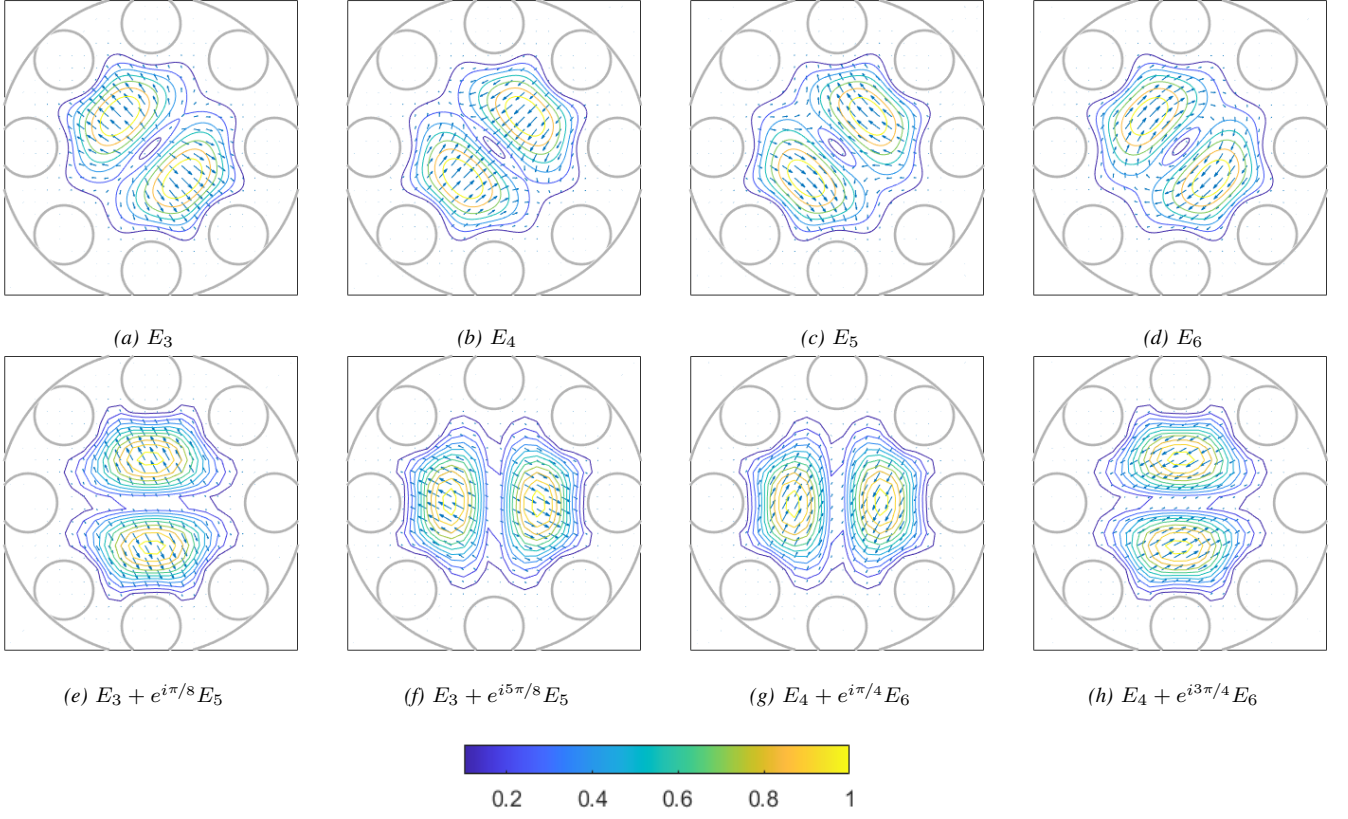


Fig. 5: Transverse electric field profiles for the second degenerate mode group guided by the waveguide under test. (a) to (d) show the profiles as obtained from the FDFD model. Superpositions of these modes give the linearly polarised modes shown in (e) to (g). The structure of the PCF is shown in grey, the magnitude of the electric field is shown as a contour map, and the polarisation of the electric field is shown using a quiver plot.

A composite error metric is required to optimise both the overlap integral and the power coupling into the target mode. A number of approaches can be taken, and here it was chosen to maximise Eq. 8. The hyperparameter γ is set by the user, allowing a balance to be struck between the two constituent error metrics. In this case a value of $\gamma = 10$ was taken, which yields overlap integrals in excess of 0.99.

$$Err_{Composite} = Err_{Overlap}^\gamma Err_{Power} \quad (8)$$

The DS algorithm is used to generate an appropriate hologram. Each iteration consists of randomly choosing a hologram pixel, randomly altering the phase delay it imposes on incident light, and calculating the new replay field. In cases where the error metric has improved the pixel change is adopted, and in cases where the error metric has deteriorated the pixel change is rejected. This iterative routine is illustrated Fig. 6.

Very high-quality replay fields can be produced using the DS algorithm at the expense of it being slow to run. It has been recognised [50] that a complete Fourier transform does not need to be performed at every iteration. Instead, the change in the replay field due to a single pixel change ΔD at position (x', y') can be calculated from Eq. 9. The update step is then of complexity $O(N_x N_y)$ instead of $O(N_x N_y \log(N_x N_y))$. This is particularly powerful if a ROI is used, as only the pixels within the ROI then need to be updated. Christopher et al. have shown that randomly selecting pixels and assigning random

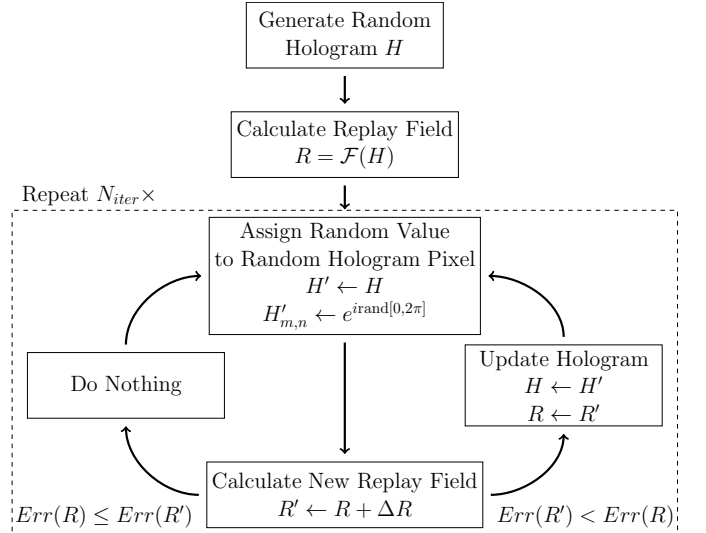


Fig. 6: The Direct Search (DS) algorithm. Calculation of ΔR using Eq. 9 gives the standard DS algorithm. It shall be shown that, when generating holograms for exciting fibre modes, the use of Eq. 12 to calculate ΔR and only considering hologram pixel values of ± 1 gives improved results.

values to these is sub-optimal, and that careful selection of the next pixel to be altered [53] and careful selection of the value it is set to [54], [55] can significantly improve both execution times and convergent error.

$$\Delta R(u, v) = \frac{1}{\sqrt{N_x N_y}} \Delta D(x', y') e^{2\pi i \left(\frac{ux'}{N_x} + \frac{vy'}{N_y} \right)} \quad (9)$$

Several further improvements are suggested here to exploit the unique characteristics of waveguide modes. Firstly, it is recognised that the field profiles of the obtained modes are real-valued to within a global phase shift, i.e. they lie on a straight line on an Argand diagram. This is a property that is generally true of guided modes in weakly guiding geometries, and is similarly true in this case where LP modes have been constructed. Secondly, it is recognised that each of the obtained modes have east-west and north-south planes of symmetry or antisymmetry (this can be observed by inspecting the target scalar modes illustrated in Fig. 9). Mathematically, a plane of symmetry corresponds to the image being described by an even-valued function along the axis of interest, and a plane of antisymmetry corresponds to the image being described by an odd-valued function along the axis of interest. Considering the Fourier transform of a real-valued function,

$$F(u, v) = \int_{-\infty}^{\infty} \int_{-\infty}^{\infty} f(x, y) e^{-2\pi i(xu - yv)} dx dy \quad (10)$$

Applying Euler's formula this can be expressed in terms of even cosine and odd sine functions

$$\begin{aligned} F(u, v) = & \int_{-\infty}^{\infty} \int_{-\infty}^{\infty} f(x, y) [\cos(2\pi xu) \cos(2\pi yv) \\ & - \sin(2\pi xu) \sin(2\pi yv)] dx dy \\ & + i \int_{-\infty}^{\infty} \int_{-\infty}^{\infty} f(x, y) [\sin(2\pi xu) \cos(2\pi yv) \\ & + \cos(2\pi xu) \sin(2\pi yv)] dx dy \quad (11) \end{aligned}$$

The integral of the product of an odd function and an even function evaluated over the entire domain tends to zero, allowing various terms in this equation to be eliminated depending on the planes of symmetry observed in the mode. It can hence be shown that any symmetry or antisymmetry observed in the replay field is also present in the hologram. Explicitly,

- $R(u, v) = R(-u, v)$ so $H(x, y) = H(-x, y)$ and we define a parameter $\text{Sym}_{LR} = 1$
- $R(u, v) = -R(-u, v)$ so $H(x, y) = -H(-x, y)$ and we define a parameter $\text{Sym}_{LR} = -1$
- $R(u, v) = R(u, -v)$ so $H(x, y) = H(x, -y)$ and we define a parameter $\text{Sym}_{UD} = 1$
- $R(u, v) = -R(u, -v)$ so $H(x, y) = -H(x, -y)$ and we define a parameter $\text{Sym}_{UD} = -1$

This entails that only one quadrant of the hologram needs to be optimised by the DS algorithm. Solving for the top-left quadrant only, the update equation of Eq. 9 is revised to Eq.

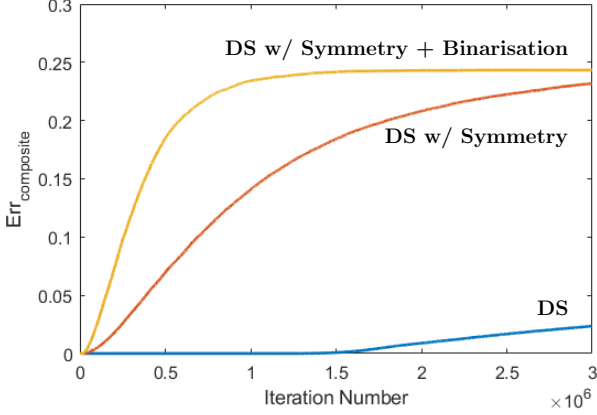
12. The other three quadrants can be inferred from the first quadrant after the calculation has been completed.

$$\begin{aligned} \Delta R(u, v) = & \frac{1}{\sqrt{N_x N_y}} \Delta D(x', y') \cdot \\ & \left(e^{-2\pi i \left(\frac{ux'}{N_x} + \frac{vy'}{N_y} \right)} + \text{Sym}_{LR} e^{-2\pi i \left(-\frac{ux'}{N_x} + \frac{vy'}{N_y} \right)} \right. \\ & \left. + \text{Sym}_{UD} e^{-2\pi i \left(\frac{ux'}{N_x} - \frac{vy'}{N_y} \right)} + \text{Sym}_{LR} \text{Sym}_{UD} e^{-2\pi i \left(-\frac{ux'}{N_x} - \frac{vy'}{N_y} \right)} \right) \quad (12) \end{aligned}$$

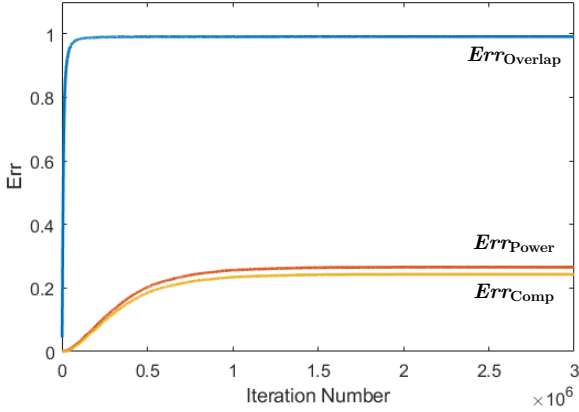
Inspection of Eq. 11 also shows that if a mode is real-valued and even along both x and y , then its hologram should also be real. Similarly, if a mode is real-valued and odd along both x and y its hologram should also be real. Given that a phase modulating SLM is used, and assuming no aberration corrections are applied, the only real values that pixels can take on are +1 and -1, and the search can hence be restricted to these values. Similarly, the hologram for a real-valued mode that is odd along one axis but even along the other should be purely imaginary. Again, given that a phase modulating SLM is used, the only imaginary values that pixels can take on are $+i$ and $-i$. But, it is noted from the form of Eq. 6 that coupling into a waveguide mode is unaffected by global phase rotations that are applied to the hologram as a whole. As such, pixel values of +1 and -1 can equally be considered. These observations are incorporated into the DS algorithm by setting the initial hologram to a random selection of +1 and -1 values. On each iteration the algorithm flips a pixel to its opposite state instead of assigning a random value. In doing this, the parameter space to be searched by the algorithm is dramatically reduced, and better results are obtained in a shorter execution time.

It has been shown that the mathematical form of the target mode profiles can be used to infer axes of symmetry in the hologram field, and hence only one quadrant needs to be optimised for. Similarly, it has been shown that only hologram pixel values of +1 or -1 need to be considered. These observations lead to substantial improvements in the speed of the hologram generation algorithm, as shown in Fig. 7a. In this case calculations have been performed for the $\text{LP}_{2,2}$ mode of a $25\mu\text{m}$ step index waveguide, but the same trends are observed in all cases.

Crucially, these speed improvements mean that it is now tractable to generate 1000×1000 pixel holograms, which was not previously possible within a reasonable time frame. Considering the example of the $\text{LP}_{2,2}$ mode given: with optimisations the algorithm converges within approximately 1.5×10^6 iterations. Without optimisations, the naïve algorithm has not yet converged after 3×10^6 iterations when it was halted prematurely. Extrapolating from these results, this naïve algorithm will likely converge after approximately 16×10^6 iterations, so a $10\times$ speed-up has been achieved. Ultimately, it is the values of $\text{Err}_{\text{Overlap}}$ and $\text{Err}_{\text{Power}}$ that are of interest, and the evolution of these parameters as the algorithm converges is shown in Fig. 7b. The MATLAB script for generating holograms using the DS algorithm has been made publicly available at [45].



(a) Convergence of the DS algorithm when i) no assumptions are made about the hologram; ii) axes of symmetry are taken into account; and iii) when both axes of symmetry and binarisation are taken into account.



(b) Evolution of the $Err_{Overlap}$, Err_{Power} and $Err_{Composite}$ as the optimised algorithm converges.

Fig. 7: Study of the convergence of the DS algorithm. The algorithm can be optimised for the generation of holograms for the excitation of waveguide modes by exploiting their symmetry properties, and by recognising that the hologram must be binary.

It is noted that horizontal and vertical symmetries of the mode profile have been exploited here, but that the mode also has diagonal symmetries. Exploitation of these diagonal symmetries could yield further improvements to the DS algorithm.

The observation that the hologram must be real-valued and hence binary if a phase-modulating SLM is used has further reaching consequences. For example, this implies that holograms for exciting LP modes can be displayed on a binary phase ferroelectric SLM without any losses being incurred. Similarly, it may also be possible to obtain high-quality replay fields using a binary amplitude modulating device such as a digital micromirror device (DMD). Both DMDs and ferroelectric SLMs have refresh rates of kHz, significantly faster than the refresh rate of nematic liquid crystal SLMs which have refresh rates of the order of 30 to 50Hz.

V. EXPERIMENTAL SETUP

The experimental setup used is illustrated in Fig. 8. On the input side a collimated beam is separated into its constituent

polarisations using a polarising beam splitter assembly before both polarisations are incident side by side on a Jasper JD8714 SLM. This is a nematic liquid crystal on silicon SLM capable of 256-level phase modulation, with a pixel pitch of $3.74\mu\text{m}$ and a resolution of $4k \times 2k$. The two separate polarisations are modulated by the SLM, and are recombined before travelling through a series of three lenses and being projected onto the input fibre facet of the waveguide under test. This configuration was used by Preece et al. [56], was subsequently also used by Carpenter et al. [51], and allows both polarisations entering the waveguide to be independently modulated. Only a single polarisation is required here, as it was possible to decompose all modes into LP modes for this waveguide. As such, the polarisation of the original collimated beam was adjusted such that all power was in a single polarisation, only a single beam is incident on the SLM, and only a single polarisation is incident on the fibre facet. The waveplates HWP1 and HWP2 ensure that the polarisation of beams is aligned with the polarisation angle of the SLM, and the waveplate HWP3 can be used to rotate the polarisation of the light entering the waveguide. The modulated beam travels through three lenses, positioned such that the entire system of lenses performs a Fourier transform.

The ideal SLM illumination profile can be calculated from the inverse Fourier transform of the target mode, and typically has a Gaussian envelope. The beam illuminating the SLM would ideally have a matching Gaussian shape. Such a beam is created by collimating the light emanating from an SMF with a lens (L1), the focal length of which has been chosen to yield a Gaussian illumination that covers most of the SLM but contains no significant power at the edge of the SLM. The focal lengths of the system of lenses after the SLM (L2, L3 and L4) has been chosen to then ensure that this illumination profile yields strong power coupling into all modes considered. It is important to note that this requires a balance to be struck, as each target mode has a slightly different ideal illumination profile. The use of the DS algorithm allows a non-uniformly illuminated SLM to be accounted for and ultimately yields improved power coupling compared to the uniform SLM illumination case.

Not all light is modulated by the SLM, so a tilt Zernike is superimposed on any displayed hologram allowing the holograms to be projected in an off-axis configuration. Unmodulated light is then spatially separated from modulated light in the fibre facet plane, allowing the system to be aligned such that only modulated light is incident on the fibre facet.

A polarising beam splitter is used to divide the light exiting the fibre into its two constituent polarisations. Off-axis holographic imaging [57], [58] is used to characterise the amplitude and phase of the light incident on each camera, and hence for each polarisation.

VI. MODE EXCITATION

Section IV discussed the use of the DS algorithm for generating a hologram to excite a given target mode. Loading an individual hologram onto the SLM will project a modulated light field onto the fibre facet that will excite the target

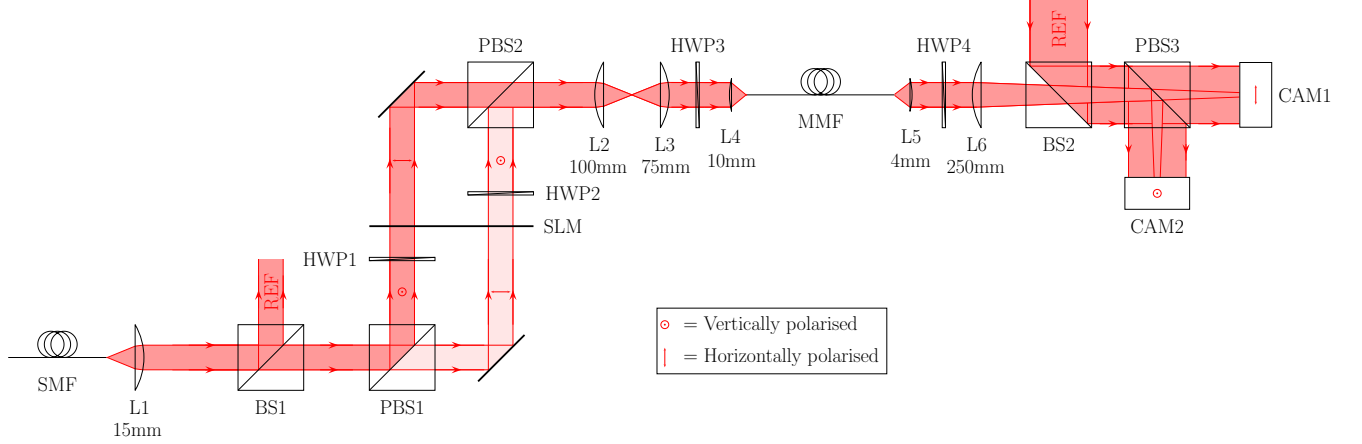


Fig. 8: Schematic of the experimental setup. An SLM is used to control light coupling into the input facet of the waveguide. The light exiting the output facet of the waveguide is characterised using off-axis holographic imaging. L = Lens; BS = Beam splitter; PBS = Polarising beam splitter; HWP = Half wave plate; CAM = Camera; SMF = Single mode fibre; MMF = Multimode fibre; SLM = Spatial light modulator; REF = Reference beam.

mode only if the experimental system is properly aligned. The system is to be aligned at the input side to correctly excite the target modes, but also requires alignment at the output side to be able to properly characterise excited modes.

The use of an off-axis interferometer allows the quality of the excited mode to be quantified using the overlap integral of Eq. 6. This is done by evaluating the overlap integral between the target mode profile and the measured mode profile. To quantify the overall alignment of the waveguide the complex output fields R_i are measured for each hologram, and the overlap with each target field T_j is taken, where i enumerates the output field considered and j enumerates the target field considered. It is recalled that the overlap integral should approach unity when the excited mode matches the target mode ($i = j$), and should approach zero when this is not the case ($i \neq j$). This allows the following waveguide alignment error metric $Err_{\text{alignment}}$ to be defined.

$$Err_{\text{alignment}} = \sum_{i=j} Err_{\text{Overlap}}(R_i, T_j) - \sum_{i \neq j} Err_{\text{Overlap}}(R_i, T_j) \quad (13)$$

The system is first coarsely aligned by hand. Next, a selection of hologram modifiers are defined, each with its own weighting, that allow the system alignment to be fine-tuned. These include the position, rotation and scaling of the hologram on the SLM; Zernikes polynomials superimposed on the hologram; position and scaling of the output; and Zernike polynomials superimposed on the output. The weightings for higher-order Zernike polynomials such as coma and trefoil tended to zero once optimised, indicating the system does not suffer from significant aberrations. Consequently, only the tilt, defocus and astigmatism Zernike polynomials were considered.

The Nelder-Mead algorithm has been used to optimise the weightings of the hologram modifiers [59] and improve the overall waveguide alignment. This algorithm is particularly well-suited as it does not require many evaluations of the align-

ment error metric (Eq. 13), which is expensive as it requires a number of measurements equal to the number of modes considered. Additionally, this algorithm does not require the gradient at each evaluated point to be known, making this algorithm appropriate for cases where an underlying analytical equation describing the problem space is not known.

Adjusting the rotation angle of the hologram allows the spatial distribution of the incident fields to be aligned with the fibre, which is oriented at an unknown angle. Similarly, the polarisation of the incident light needs to be suitably aligned. This is done by periodically stopping the execution of the alignment algorithm and manually adjusting HWP3.

After the system is fully aligned, discrete modes can be excited in the waveguide by displaying the appropriate hologram on the SLM. The left-hand column of Fig. 9 shows seven LP modes guided by the waveguide, calculated using the FDFD code described previously. The central column of Fig. 9 shows the holograms to excite these LP modes, generated using the DS algorithm. Finally, the right-hand column of Fig. 9 shows the experimentally excited mode, measured at the output of the waveguide using an off-axis interferometer. Each measured mode is visually similar to the calculated target mode.

Taking measurements with HWP4 positioned at different rotation angles confirms that, for the short lengths of waveguide considered, the polarisation of the guided mode is not altered by propagation through the waveguide and that there is minimal coupling between the excited mode and its degenerate counterparts. Once this was confirmed the half wave plate was removed.

The overlap integral between the measured mode and the target mode, shown in Table I, gives a numerical estimate of how purely the target mode is excited. All overlap integrals except for the $LP_{4,1}$ mode exceed 85%, indicating that the target mode is appropriately excited. The achieved purity is less the 99% that can theoretically be achieved by the hologram, though. First, it is noted the assumed waveguide geometry was approximated to circles and ellipses. Conse-

	Theoretical Mode Purity (%)	Measured Mode Purity (%)
$LP_{0,1}$	> 99.0	97.4
$LP_{1,1}$	> 99.0	92.5
$LP_{2,1}$	> 99.0	88.7
$LP_{0,2}$	> 99.0	91.6
$LP_{3,1}$	> 99.0	89.1
$LP_{1,2}$	> 99.0	89.2
$LP_{4,1}$	> 99.0	73.7

TABLE I: Comparison of theoretical mode purity and measured mode purity.

quent discrepancies between the calculated modes and the true propagation invariant modes partly explain the lower purity of the excited modes. Secondly, it was not possible to obtain a perfectly flat finish on the waveguide facet without disturbing the internal structure of the PCF. While the cleave angle is nominally perpendicular to the fibre axis, distortions and protrusions on the input and output facets will interact with the wavefront, also perturbing the purity of the measured mode.

The in-coupling efficiency achieved for each mode was determined by measuring the input power between lenses L2 and L3, and by measuring the output power between lenses L5 and L6. The input power measurement comprises the zeroth diffraction order as well as higher order diffraction orders. The ratio of these two measurements is then corrected for the loss in the waveguide, as calculated using the FDFD model (see Fig. 4b). The results of this calculation are shown in Table II where they are compared against the theoretical hologram efficiency. Good general agreement is observed between the theoretical excitation efficiencies and the observed excitation efficiencies for the first six modes which are within 5.5% of the theoretical excitation efficiency. These discrepancies can be attributed to factors such as Fresnel reflection losses that have not been accounted for and experimental uncertainty. The excitation efficiency for the $LP_{0,1}$ is lower than that of the other values. This is a consequence of the choice of lens performing the Fourier transform, the focal length of which favours efficient coupling into higher order modes.

The final $LP_{4,1}$ mode was excited with a particularly low purity of 73.7%, and with an excitation efficiency 14.7% lower than the theoretical excitation efficiency. It is hypothesised that this is because the mode is not truly guided in the experimental geometry due to the aforementioned discrepancies between the assumed waveguide geometry and the experimental waveguide geometry.

VII. CONCLUSIONS

We have presented an end to end approach to holographically exciting complex modes in complex geometries with high mode purity and high power efficiency. An FDFD model has been used to determine what modes are guided in a nodeless antiresonant PCF waveguide geometry. Each mode predicted by the FDFD model was able to be excited, showing that this model accurately allows the modes guided by the waveguide to be discerned.

The modes were excited using Fourier holograms generated using a DS algorithm, allowing the purity of the excited mode to be traded off with the excitation efficiency. Modifications to

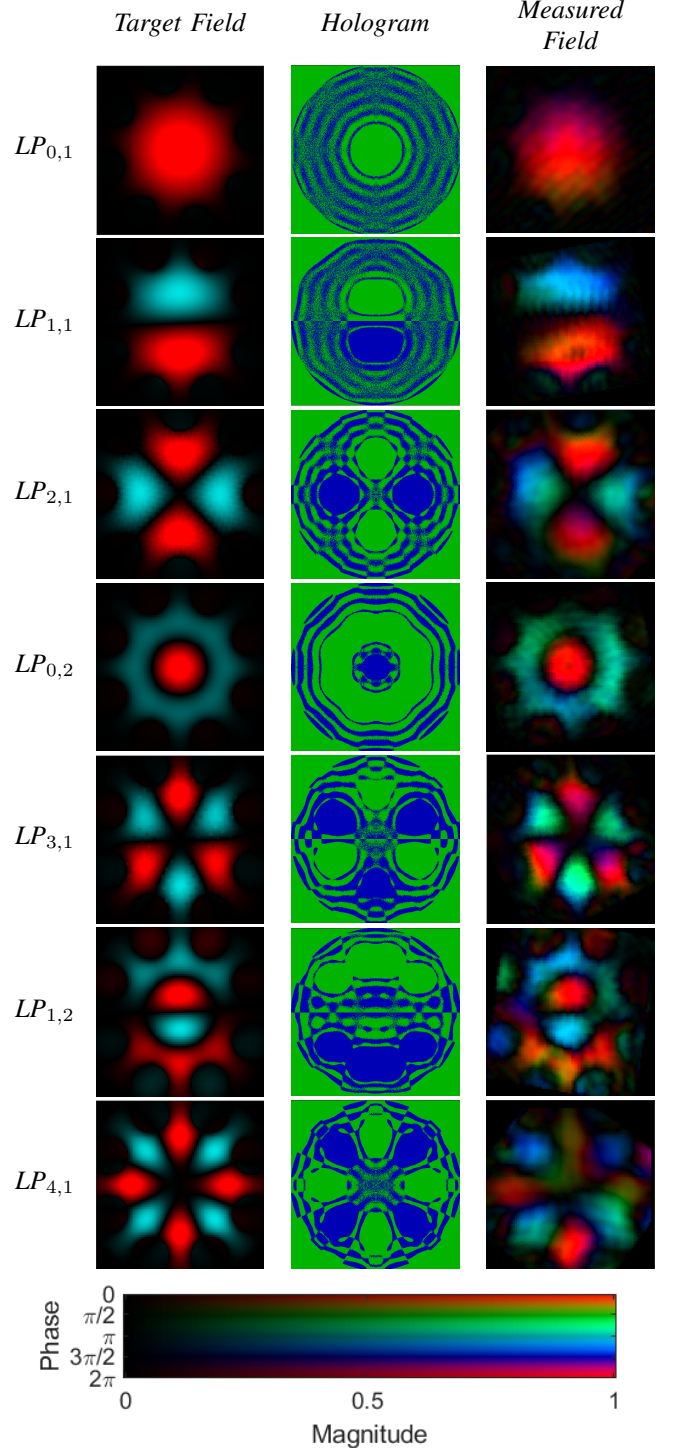


Fig. 9: (Left): Scalar target mode profile. (Centre): Hologram generated to excite target mode. (Right): Mode excited using the generated hologram, measured upon exiting the waveguide using an off-axis interferometer.

	P_{out}/P_{in} [measured] (%)	Loss in 8cm [from FDFD model] (%)	Measured Efficiency $P_{out}/(P_{in}(1-Loss))$ (%)	Theoretical Efficiency [from hologram] (%)	Difference (%)
$LP_{0,1}$	13.3	7.4	14.4	17.5	-3.1
$LP_{1,1}$	17.8	17.4	21.6	22.2	-0.7
$LP_{2,1}$	18.2	29.5	25.8	31.3	-5.5
$LP_{0,2}$	23.3	33.8	35.2	33.0	2.2
$LP_{3,1}$	17.6	43.5	31.2	35.2	-4.0
$LP_{1,2}$	12.7	66.4	37.7	37.4	0.3
$LP_{4,1}$	9.3	66.5	27.8	42.5	-14.7

TABLE II: Comparison of theoretical excitation efficiency and measured excitation efficiency.

the DS algorithm were proposed based on known properties of LP modes. These improvements yielded execution times that were ten faster, allowing high-quality 1000×1000 pixel holograms to be generated.

The excitation purity of each guided mode exceeded 88%, and an improved model for the waveguide geometry will likely enable the excitation of even purer modes. The obtained holograms allow up to 37% of power to be coupled into the target mode, significantly more than what is possible with alternative approaches [24], [25]. These efficiencies can be further improved upon if only a single mode is to be excited, as the illumination of the SLM and chosen lenses can be tailored to yield even larger efficiency values.

While a single waveguide geometry has been considered here, care has been taken to ensure the approaches described in this paper are general, and these techniques can be used to excite modes in any arbitrary waveguide geometry. Excitation of discrete modes in these arbitrary geometries will enable spatially-resolved sensing of photochemical processes in liquid-filled PCF microreactors [60], as well as optical trapping of sensing microparticles along a HC-PCF core [4], [61].

ACKNOWLEDGEMENTS

The authors wish to thank the Engineering and Physical Sciences Research Council (EP/L015889/1, EP/T008369/1, EP/L016567/1, EP/P030181/1 and EP/T008369/1) and the Leverhulme Trust (Research Project Grant RPG-2018-256) for financial support during the period of this research.

REFERENCES

- [1] R. Ryf, S. Randel, A. H. Gnauck, C. Bolle, A. Sierra, S. Mumtaz, M. Esmaelpour, E. C. Burrows, R. Essiambre, P. J. Winzer, D. W. Peckham, A. H. McCurdy, and R. Lingle, "Mode-division multiplexing over 96 km of few-mode fiber using coherent 6×6 MIMO processing," *Journal of Lightwave Technology*, vol. 30, no. 4, pp. 521–531, 2012.
- [2] J. Carpenter, B. C. Thomsen, and T. D. Wilkinson, "Degenerate mode-group division multiplexing," *Journal of Lightwave Technology*, vol. 30, no. 24, pp. 3946–3952, 2012.
- [3] J. Carpenter and T. D. Wilkinson, "All optical mode-multiplexing using holography and multimode fiber couplers," *Journal of Lightwave Technology*, vol. 30, no. 12, pp. 1978–1984, 2012.
- [4] O. A. Schmidt, T. G. Euser, and P. S. Russell, "Mode-based microparticle conveyor belt in air-filled hollow-core photonic crystal fiber," *Opt. Express*, vol. 21, no. 24, pp. 29 383–29 391, 2013.
- [5] B. M. Trabold, A. Abdolvand, T. G. Euser, A. M. Walser, and P. S. Russell, "Amplification of higher-order modes by stimulated Raman scattering in H₂-filled hollow-core photonic crystal fiber," *Opt. Lett.*, vol. 38, no. 5, pp. 600–602, Mar 2013. [Online]. Available: <http://ol.osa.org/abstract.cfm?URI=ol-38-5-600>
- [6] G. Epple, N. Y. Joly, T. G. Euser, P. S. Russell, and R. Löw, "Effect of stray fields on Rydberg states in hollow-core PCF probed by higher-order modes," *Opt. Lett.*, vol. 42, no. 17, pp. 3271–3274, Sep 2017. [Online]. Available: <http://ol.osa.org/abstract.cfm?URI=ol-42-17-3271>
- [7] P. K. Tien and R. Ulrich, "Theory of prism-film coupler and thin-film light guides," *J. Opt. Soc. Am.*, vol. 60, no. 10, pp. 1325–1337, 1970.
- [8] D. Sarid, P. J. Cressman, and R. L. Holman, "High-efficiency prism coupler for optical waveguides," *Applied Physics Letters*, vol. 33, no. 6, pp. 514–515, 1978.
- [9] K.-S. Chiang and S. Cheng, "Technique of applying the prism-coupler method for accurate measurement of the effective indices of channel waveguides," *Optical Engineering*, vol. 47, no. 3, pp. 1 – 4, 2008.
- [10] M. Neviere, R. Petit, and M. Cadilhac, "About the theory of optical grating coupler-waveguide systems," *Optics Communications*, vol. 8, no. 2, pp. 113 – 117, 1973.
- [11] X. Chen, C. Li, C. K. Y. Fung, S. M. G. Lo, and H. K. Tsang, "Apodized waveguide grating couplers for efficient coupling to optical fibers," *IEEE Photonics Technology Letters*, vol. 22, no. 15, pp. 1156–1158, 2010.
- [12] R. Marchetti, C. Lacava, A. Khokhar, X. Chen, I. Cristiani, D. J. Richardson, G. T. Reed, P. Petropoulos, and P. Minzioni, "High-efficiency grating-couplers: Demonstration of a new design strategy," *Scientific Reports*, vol. 7, no. 1, pp. 1–8, 2017.
- [13] Z. Haas and M. A. Santoro, "A mode-filtering scheme for improvement of the bandwidth-distance product in multimode fiber systems," *Journal of Lightwave Technology*, vol. 11, no. 7, pp. 1125–1131, 1993.
- [14] L. Raddatz, I. H. White, D. G. Cunningham, and M. C. Nowell, "Increasing the bandwidth-distance product of multimode fibre using offset launch," *Electronics Letters*, vol. 33, no. 3, pp. 232–233, 1997.
- [15] —, "An experimental and theoretical study of the offset launch technique for the enhancement of the bandwidth of multimode fiber links," *J. Lightwave Technol.*, vol. 16, no. 3, p. 324, 1998.
- [16] N. K. Fontaine, R. Ryf, J. Bland-Hawthorn, and S. G. Leon-Saval, "Geometric requirements for photonic lanterns in space division multiplexing," *Opt. Express*, vol. 20, no. 24, pp. 27 123–27 132, 2012.
- [17] S. G. Leon-Saval, N. K. Fontaine, and R. Amezcua-Correa, "Photonic lantern as mode multiplexer for multimode optical communications," *Optical Fiber Technology*, vol. 35, pp. 46 – 55, 2017.
- [18] A. M. Velázquez-Benítez, J. E. Antonio-López, J. C. Alvarado-Zacarias, N. K. Fontaine, R. Ryf, H. Chen, J. Hernández-Cordero, P. Sillard, C. Okonkwo, S. G. Leon-Saval, and R. Amezcua-Correa, "Scaling photonic lanterns for space-division multiplexing," *Scientific Reports*, vol. 8, no. 1, pp. 1–9, 2018.
- [19] S. Berdagué and P. Facq, "Mode division multiplexing in optical fibers," *Appl. Opt.*, vol. 21, no. 11, pp. 1950–1955, 1982.
- [20] G. Stepniak, L. Maksymiuk, and J. Siuzdak, "Binary-phase spatial light filters for mode-selective excitation of multimode fibers," *Journal of Lightwave Technology*, vol. 29, no. 13, pp. 1980–1987, 2011.
- [21] D. Flamm, D. Naidoo, C. Schulze, A. Forbes, and M. Duparré, "Mode analysis with a spatial light modulator as a correlation filter," *Optics Letters*, vol. 37, no. 13, p. 2478, 2012.
- [22] D. Flamm, C. Schulze, D. Naidoo, S. Schroter, A. Forbes, and M. Duparré, "All-digital holographic tool for mode excitation and analysis in optical fibers," *Journal of Lightwave Technology*, vol. 31, no. 7, pp. 1023–1032, 2013.
- [23] J. Carpenter and T. D. Wilkinson, "Characterization of multimode fiber by selective mode excitation," *Journal of Lightwave Technology*, vol. 30, no. 10, pp. 1386–1392, 2012.
- [24] T. G. Euser, G. Whyte, M. Scharrer, J. S. Y. Chen, A. Abdolvand, J. Nold, C. F. Kaminski, and P. S. Russell, "Dynamic control of higher-order modes in hollow-core photonic crystal fibers," *Opt. Express*, vol. 16, no. 22, pp. 17 972–17 981, 2008.
- [25] A. Ruskuc, P. Koehler, M. A. Weber, A. Andres-Arroyo, M. H. Frosz, P. S. Russell, and T. G. Euser, "Excitation of higher-order modes in optofluidic photonic crystal fiber," *Opt. Express*, vol. 26, no. 23, pp. 30 245–30 254, 2018.
- [26] Y. Y. Wang, N. V. Wheeler, F. Couny, P. J. Roberts, and F. Benabid, "Low loss broadband transmission in hypocycloid-core kagome hollow-

- core photonic crystal fiber,” *Opt. Lett.*, vol. 36, no. 5, pp. 669–671, 2011.
- [27] W. J. Wadsworth, R. M. Percival, G. Bouwmans, J. C. Knight, and P. S. J. Russell, “High power air-clad photonic crystal fibre laser,” *Opt. Express*, vol. 11, no. 1, pp. 48–53, Jan 2003.
- [28] H. Sakr, Y. Chen, G. T. Jasion, T. D. Bradley, J. R. Hayes, H. C. H. Mulvad, I. A. Davidson, E. Numkam Fokoua, and F. Poletti, “Hollow core optical fibres with comparable attenuation to silica fibres between 600 and 1100 nm,” *Nature Communications*, vol. 11, no. 1, pp. 1–10, 2020.
- [29] A. M. Cubillas, S. Unterkofler, T. G. Euser, B. J. M. Etzold, A. C. Jones, P. J. Sadler, P. Wasserscheid, and P. S. J. Russell, “Photonic crystal fibres for chemical sensing and photochemistry,” *Chemical Society Reviews*, vol. 42, no. 22, p. 8629, 2013.
- [30] P. S. J. Russell, P. Hölzer, W. Chang, A. Abdolvand, and J. Travers, “Hollow-core photonic crystal fibres for gas-based nonlinear optics,” *Nature Photonics*, vol. 8, no. 4, pp. 278–286, 2014.
- [31] A. D. Pryamikov, A. S. Biriukov, A. F. Kosolapov, V. G. Plotnichenko, S. L. Semjonov, and E. M. Dianov, “Demonstration of a waveguide regime for a silica hollow-core microstructured optical fiber with a negative curvature of the core boundary in the spectral region 3.5 μm ,” *Optics express*, vol. 19, no. 2, pp. 1441–1448, 2011.
- [32] N. Litchinitser, A. Abeeluck, C. Headley, and B. Eggleton, “Antiresonant reflecting photonic crystal optical waveguides,” *Optics letters*, vol. 27, no. 18, pp. 1592–1594, 2002.
- [33] F. Poletti, “Nested antiresonant nodeless hollow core fiber,” *Opt. Express*, vol. 22, no. 20, pp. 23 807–23 828, Oct 2014.
- [34] H. Sakr, Y. Hong, T. D. Bradley, G. T. Jasion, J. R. Hayes, H. Kim, I. A. Davidson, E. N. Fokoua, Y. Chen, K. R. H. Bottrill, N. Taengnoi, N. V. Wheeler, P. Petropoulos, D. J. Richardson, and F. Poletti, “Interband short reach data transmission in ultrawide bandwidth hollow core fiber,” *Journal of Lightwave Technology*, vol. 38, no. 1, pp. 159–165, 2020.
- [35] M. S. Habib, C. Markos, and R. Amezcua-Correa, “Impact of cladding elements on the loss performance of hollow-core anti-resonant fibers,” *Opt. Express*, vol. 29, no. 3, pp. 3359–3374, Feb 2021.
- [36] A. Taranta, E. N. Fokoua, S. A. Mousavi, J. R. Hayes, T. D. Bradley, G. T. Jasion, and F. Poletti, “Exceptional polarization purity in antiresonant hollow-core optical fibres,” *Nature Photonics*, vol. 14, pp. 504–510, 2020.
- [37] J.-L. Archambault, R. Black, S. Lacroix, and J. Bures, “Loss calculations for antiresonant waveguides,” *Journal of Lightwave Technology*, vol. 11, no. 3, pp. 416–423, 1993.
- [38] M. A. Finger, N. Y. Joly, T. Weiss, and P. S. J. Russell, “Accuracy of the capillary approximation for gas-filled kagomé-style photonic crystal fibers,” *Optics Letters*, vol. 39, no. 4, p. 821, 2014.
- [39] Lumerical Inc., *MODE Product Reference Manual*, Accessed: 12 September 2021. [Online]. Available: <https://support.lumerical.com/hc/en-us/articles/360020687354-MODE-product-reference-manual>
- [40] COMSOL, *COMSOL Multiphysics Reference Manual*, Accessed: 12 September 2021. [Online]. Available: https://doc.comsol.com/5.5/doc/com.comsol.help.comsol/COMSOL_ReferenceManual.pdf
- [41] A. Oskooi, D. Roundy, M. Ibanescu, P. Bermel, J. Joannopoulos, and S. Johnson, “MEEP: A flexible free-software package for electromagnetic simulations by the FDTD method,” *Computer Physics Communications*, vol. 181, pp. 687–702, 2010.
- [42] W. Shin and S. Fan, “Choice of the perfectly matched layer boundary condition for frequency-domain maxwell’s equations solvers,” *Journal of Computational Physics*, vol. 231, no. 8, pp. 3406 – 3431, 2012.
- [43] Z. Zhu and T. G. Brown, “Full-vectorial finite-difference analysis of microstructured optical fibers,” *Opt. Express*, vol. 10, no. 17, pp. 853–864, 2002.
- [44] C.-P. Yu and H.-C. Chang, “Compact finite-difference frequency-domain method for the analysis of two-dimensional photonic crystals,” *Opt. Express*, vol. 12, no. 7, pp. 1397–1408, 2004.
- [45] R. Mouthaan, “PCF mode excitation,” <https://github.com/ralfmouthaan/Paper-PCF-Mode-Excitation>, 2021.
- [46] W. P. Huang and C. L. Xu, “Simulation of three-dimensional optical waveguides by a full-vector beam propagation method,” *IEEE Journal of Quantum Electronics*, vol. 29, no. 10, pp. 2639–2649, 1993.
- [47] P. Lusse, P. Stuwe, J. Schüle, and H. Unger, “Analysis of vectorial mode fields in optical waveguides by a new finite difference method,” *Journal of Lightwave Technology*, vol. 12, no. 3, pp. 487–494, 1994.
- [48] E. Marcatili and R. Schmeltzer, “Hollow metallic and dielectric waveguides for long distance optical transmission and lasers,” *Bell System Technical Journal*, 1964.
- [49] S. Rothe, H. Radner, N. Koukourakis, and J. W. Czarske, “Transmission matrix measurement of multimode optical fibers by mode-selective excitation using one spatial light modulator,” *Applied Sciences (Switzerland)*, vol. 9, no. 1, 2019.
- [50] J. A. Carpenter and T. D. Wilkinson, “Graphics processing unit-accelerated holography by simulated annealing,” *Optical Engineering*, vol. 49, no. 9, pp. 1 – 7, 2010.
- [51] J. Carpenter, B. J. Eggleton, and J. Schröder, “110x110 optical mode transfer matrix inversion,” *Optics Express*, vol. 22, no. 1, p. 96, 2014.
- [52] J. W. Goodman, *Introduction to Fourier Optics*, 3rd ed. Roberts & Company, 2005.
- [53] P. J. Christopher, J. D. Lake, D. Dong, H. J. Joyce, and T. D. Wilkinson, “Improving holographic search algorithms using sorted pixel selection,” *J. Opt. Soc. Am. A*, vol. 36, no. 9, pp. 1456–1462, 2019.
- [54] P. J. Christopher, Y. Wang, and T. D. Wilkinson, “Predictive search algorithm for phase holography,” *J. Opt. Soc. Am. A*, vol. 36, no. 12, pp. 2068–2075, 2019.
- [55] P. J. Christopher, R. Mouthaan, G. S. Gordon, and T. D. Wilkinson, “Holographic predictive search: Extending the scope,” *Optics Communications*, vol. 467, p. 125701, 2020.
- [56] D. Preece, S. Keen, E. Botvinick, R. Bowman, M. Padgett, and J. Leach, “Independent polarisation control of multiple optical traps,” *Optics express*, vol. 16, no. 20, pp. 15 897–15 902, 2008.
- [57] M. Liebling, T. Blu, and M. Unser, “Complex-wave retrieval from a single off-axis hologram,” *J. Opt. Soc. Am. A*, vol. 21, no. 3, pp. 367–377, 2004.
- [58] N. Verrier and M. Atlan, “Off-axis digital hologram reconstruction: Some practical considerations,” *Applied Optics*, vol. 50, no. 34, 2011.
- [59] W. H. Press, S. A. Teukolsky, W. T. Vetterling, and B. P. Fannery, *Numerical Recipes*, 3rd ed. Cambridge University Press, 2007.
- [60] G. O. S. Williams, J. S. Y. Chen, T. G. Euser, P. S. Russell, and A. C. Jones, “Photonic crystal fibre as an optofluidic reactor for the measurement of photochemical kinetics with sub-picomole sensitivity,” *Lab Chip*, vol. 12, pp. 3356–3361, 2012.
- [61] D. S. Bykov, O. A. Schmidt, T. G. Euser, and P. S. J. Russell, “Flying particle sensors in hollow-core photonic crystal fibre,” *Nature Photonics*, vol. 9, no. 7, pp. 461–465, 2015.